

Parametric down-conversion photon pair source on a nanophotonic chip

Xiang Guo,¹ Chang-Ling Zou,¹ Carsten Schuck,¹ Hojoong Jung,¹ Risheng Cheng,¹ and Hong X. Tang¹

¹*Department of Electrical Engineering, Yale University, New Haven, Connecticut 06511, USA*

Quantum photonic chips, which integrate quantum light sources alongside active and passive optical elements, as well as single photon detectors, show great potential for photonic quantum information processing and quantum technology. Mature semiconductor nanofabrication processes allow for scaling such photonic integrated circuits to on-chip networks of increasing complexity. Second order nonlinear materials are the method of choice for generating photonic quantum states in the overwhelming part of linear optic experiments using bulk components but integration with waveguide circuitry on a nanophotonic chip proved to be challenging. Here we demonstrate such an on-chip parametric down-conversion source of photon pairs based on second order nonlinearity in an Aluminum nitride microring resonator. We show the potential of our source for quantum information processing by measuring high-visibility antibunching of heralded single photons with nearly ideal state purity. Our down conversion source operates with high brightness and low noise, yielding pairs of correlated photons at MHz-rates with high coincidence-to-accidental ratio. The generated photon pairs are spectrally far separated from the pump field, providing good potential for realizing sufficient on-chip filtering and monolithic integration of quantum light sources, waveguide circuits and single photon detectors.

Keywords: nanofabrication, quantum photonic chip, second order nonlinear material, single photon source

INTRODUCTION

Photons are excellent quantum information carriers because they combine high-speed with long coherence times at room temperature [1, 2]. Photon pair sources based on spontaneous parametric down conversion (SPDC) have enabled major advances in photonic quantum computation and communication [3, 4]. Quantum teleportation [5–7], multi-photon manipulation [8–14], quantum algorithms [15–19] and loophole-free tests of local realism [20, 21] were all achieved with SPDC-photons generated in materials with a strong second order ($\chi^{(2)}$) optical nonlinearity. Common nonlinear crystals employed for SPDC, e.g. lithium niobate (LiNbO_3), are centimeter-sized and not yet compatible with standard nanofabrication technologies [22–24]. Meanwhile, silicon-based nanophotonic chips have emerged, which leverage mature semiconductor fabrication processes to provide a stable and scalable solution for optical quantum information processing [2, 25–28]. However, the generation of SPDC photons for current experiments with silicon photonic chips is still realized in separate bulk optic setups. One alternative approach resorts to exploiting the $\chi^{(3)}$ optical nonlinearity of silicon, which allows for generating correlated photon pairs via the process of spontaneous four wave mixing (SFWM) [29–31]. Integrating an optically pumped source of correlated photons with waveguides and detectors on the same chip requires one, however, to efficiently separate the generated signal and idler photons from the co-propagating classical pump field. In the SFWM process the generated photon pairs are spectrally separated by only a few nanometers from the optical pump wavelength, which hence makes sufficient filtering and integration of such sources with

detectors on one chip a challenging task. Because on-chip pump light suppression requires sophisticated techniques [32] a variety of important physical processes could only be realized using SFWM in combination with off-chip filtering, e.g. in source multiplexing [33], on-chip quantum interference [31], and entanglement [34–36]. SPDC offers better prospects for efficient pump light suppression and consequently integrating source and detector on the same chip. Efficient filtering can for example be achieved by implementing a down conversion photon pair source on a silicon substrate, where the pump light is in the visible wavelength range and photon pairs are generated at infrared wavelengths. The material absorption of silicon for visible light is then large enough (1740 dB/cm) to guarantee efficient suppression of undesired pump light before SPDC photons reach an on-chip detector.

Aluminum nitride (AlN) is a new material suitable for scalable photonic integrated circuits [37, 38]. Its strong intrinsic second order nonlinearity ($\chi^{(2)}$) not only shows great potential for realizing on-chip photon pair sources based on SPDC [38], but also permits integrated low-loss, high-speed electro-optic (EO) phase modulation [37]. Here we demonstrate an integrated SPDC photon pair source using a high quality factor (Q) AlN microring resonator. For compatibility with telecommunication technology we realize nonlinear conversion of visible wavelength (775 nm) pump photons to telecom wavelength (1550 nm) photon pairs. High refractive index contrast between the AlN-waveguides and a silicon dioxide (SiO_2) cladding layer allows for small device footprint and enables dense integration on silicon handles. The generated photon pairs are characterized by waveguide coupled superconducting single photon detectors (SSPD) integrated on a dedicated chip. We achieve high photon

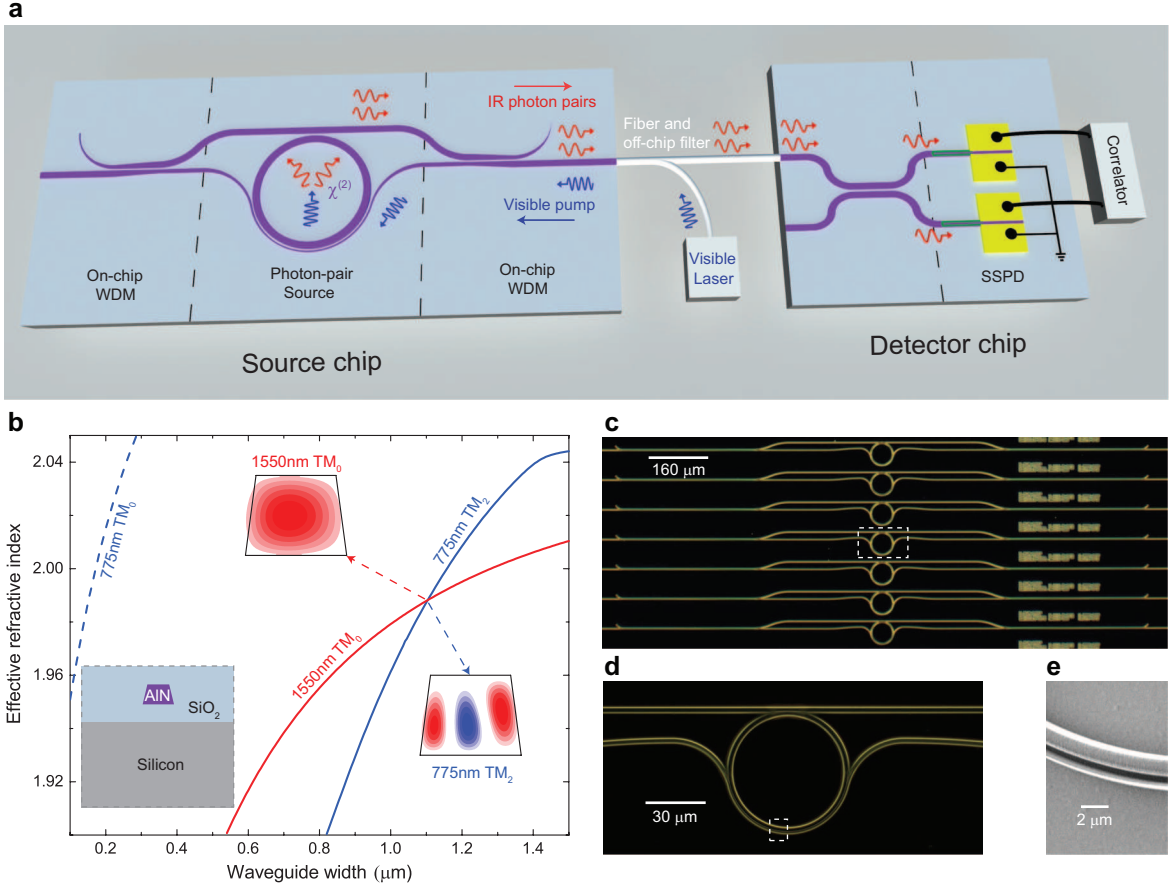


FIG. 1: On-chip spontaneous parametric down conversion photon pair source. (a) Schematic illustration of an on-chip photon pair source based on a $\chi^{(2)}$ nonlinearity connected to superconducting single photon detectors (SSPD) on another chip. Higher energy pump photons (visible wavelengths) are coupled into a microring resonator and the generated lower energy photon pairs (IR wavelengths) are randomly split on the detector chip for coincidence measurements with integrated SSPDs. A fiber coupled silicon filter (labeled as off-chip filter) is used to reject the remaining pump light reflected back from fiber-to-chip interface. (b) Effective refractive indices of modes in microring. Phase match condition is satisfied with waveguide width around $1.10\ \mu\text{m}$. Lower left inset: the cross-section of the AlN waveguide. Insets on the right: The electric field profiles at the cross-section of microring of two phase-matched modes. (c-e) Device images of AlN down conversion photon pair source. The white dashed box shows the zoom-in region. (c) Optical image of an array of microring photon pair source with on-chip WDMs. (d) Zoom-in of a single microring resonator with both IR (top) and visible (bottom) bus waveguides. (e) SEM picture showing the coupling region of visible light bus waveguide (narrow) with microring resonator (wide).

pair production rates of $3\ \text{MHz/mW}$ ($5.8\ \text{MHz/mW}$) for degenerate (non-degenerate) down conversion. The overall photon pair emission rate is more than $20\ \text{MHz/mW}$, which is comparable to the state-of-the-art bulk optic photon pair sources [24]. In terms of the spectral brightness, the demonstrated AlN microring SPDC source is much brighter than conventional waveguide or bulk crystal based sources. We observe high-visibility antibunching of heralded single photons, characterized by second order intensity correlations of $g_h^{(2)}(0) = 0.088 \pm 0.004$. The suitability of our SPDC source for quantum information applications is further highlighted by nearly ideal purity of the heralded photons, which we demonstrate in self-correlation measurements of the idler photons.

MATERIALS AND METHODS

Experimental setup and device engineering

The device is shown in Fig. 1a. We realize the SPDC source as a high quality factor AlN microring resonator, which enhances the pump photon interaction with the material's $\chi^{(2)}$ nonlinearity [39]. This allows for producing down-conversion photon pairs with long-coherence time at low optical pump power. Here, the visible wavelength pump laser field is guided into the microring resonator via a narrow wrap-around waveguide, while the generated IR photon pairs are coupled out via a wider bus waveguide. We design an on-chip wavelength division multiplexer (WDM), which guides IR photons back into the optical fiber towards the detectors. After passing through a fiber coupled silicon filter, the residual visible pump photons are rejected while IR photons are guided

to waveguide coupled superconducting single photon detectors (SSPD), which are integrated on a separate chip [27, 28, 40] inside a cryostat. Waveguide directional couplers on this detection chip allow for 50/50 splitting of photon pairs before detection with the SSPDs and signal analysis with time correlated single photon counting (TCSPC) electronics.

The lower left inset in Fig. 1b shows the cross-section of the AlN chip. AlN forms the core of the waveguide while SiO₂ acts as a low refractive index cladding layer, on top of the silicon substrate. A degenerate (non-degenerate) SPDC process involves one optical pump mode in the visible wavelength band and one (two) signal and idler modes in the IR wavelength band. Energy conservation implies the condition $\omega_{\text{vis}} = \omega_{\text{IR},1} + \omega_{\text{IR},2}$, while momentum conservation requires $m_{\text{vis}} = m_{\text{IR},1} + m_{\text{IR},2}$, where ω_x and m_x ($x = \text{vis}, \text{IR}, 1$ or $\text{IR}, 2$) are the frequencies and azimuthal numbers of the visible and IR modes, respectively (for degenerate SPDC $\omega_{\text{IR},1} = \omega_{\text{IR},2}$ and $m_{\text{IR},1} = m_{\text{IR},2}$). To fulfill these two conditions and realize efficient nonlinear conversion, it is necessary to match the effective refractive indices $n_{\text{eff}} = m_x c / \omega_x r$ (c is the speed of light in vacuum and r is the radius of the microring) of the visible pump and IR signal and idler modes. This phase matching condition can be satisfied for a higher order transverse magnetic (TM) visible wavelength pump mode and fundamental TM (TM₀) signal and idler modes in the IR [38, 41]. In Fig. 1b we show how this effective refractive index matching is achieved for a 775 nm TM₂ mode and a 1550 nm TM₀ mode by engineering the waveguide-width of the AlN microring. In the right two insets of Fig. 1b the corresponding mode profiles in a 1.10 μm width waveguide are shown.

The high refractive index contrast between waveguide (AlN) and cladding (SiO₂) materials allows for a small device footprint and dense integration. In Fig. 1c we show an optical micrograph of an array of AlN microring photon pair sources integrated with on-chip WDMs. Two independent waveguide channels are designed for visible and IR light, respectively (Fig. 1d). To excite the visible wavelength TM₂ mode inside the ring resonator we utilize a narrow wrap-around waveguide. Adjusting the gap between the ring and the wrap-around waveguide as well as the wrap-around waveguide width it is possible to adiabatically couple the TM₀ pump mode of the feed waveguide to the TM₂ mode of the microring under critical coupling conditions. As long as the gap between the wrap-around waveguide and the microring is large enough, the existence of this narrow waveguide will not deteriorate the quality factor for the ring resonator's IR modes (see supplementary section I). The wrap-around waveguide is tapered down to 100 nm, as shown in the SEM image of the coupling region (Fig. 1e) while the coupling gap between wrap-around waveguide and microring is 500 nm.

Device fabrication and measurement

A 1 μm thin AlN film is sputtered on a commercial oxide-

on-silicon wafer. We use FOX-16 resist and define patterns in electron beam lithography. After development in MF312 developer, Cl₂/BCl₃/Ar chemistry is used to etch into the AlN layer. The chip is then coated with a 2.5 μm of PECVD oxide cladding layer as protection during subsequent polishing steps. The device is finally annealed in an O₂ atmosphere for 5 h at 950 C to improve the quality of PECVD oxide. The detector chip is fabricated from a commercial 330 nm SiN-on-insulator wafer onto which we sputter an 8 nm thin film of NbTiN. Electrode pads are defined in PMMA resist via electron beam lithography followed by gold deposition and lift-off in acetone. In a second electron beam lithography step the SSPD nanowires are patterned in HSQ negative tone resist and transferred into the NbTiN layer using CF₄ chemistry. In the third and final electron beam lithography step the SiN waveguides are written in ZEP positive tone resist followed by a timed reactive ion etch in CHF₃/O₂ chemistry.

We use a continuous-wave visible wavelength laser (TLB-6712) to pump the SPDC source. A fiber coupled silicon absorber (OZ optics) is used to filter out the pump light reflected from fiber-to-chip interface. We achieve 80 dB attenuation for pump light at 3 dB insertion loss for IR light. For the degenerate SPDC coincidence measurement, a band-pass tunable filter is used to spectrally filter out the degenerate down conversion photons. For the measurements of the SPDC thermal state, a dense wavelength division multiplexer (DWDM) is used to select the idler branch from the nearest non-degenerate down conversion photon pair. The photons are then sent into the detector chip, where superconducting single photon detectors are integrated with a 50/50 directional coupler for self-correlation measurements [28]. Electrical signals from the on-chip detectors are sent into a Time-Correlated Single Photon Counting (TCSPC) system (PicoHarp 300) for time tagging [42]. For non-degenerate cross-correlation measurements, a DWDM is used to separate signal and idler photons, which are then sent to two separate on-chip detectors for coincidence measurement.

RESULTS AND DISCUSSION

Characterization of on-chip down-conversion source

We first characterize the classical performances of the microring resonator. Figure 2a shows the microring transmission spectrum for visible light in a slightly under-coupled configuration (a critically-coupled spectrum is shown in the supplementary section I). Figure 2b shows the transmission spectrum for IR light, when the bus waveguide is critically-coupled to the microring resonator. The two spectra show how the TM_{2,2N} mode at 775 nm aligns with the TM_{0,N} mode at twice the wavelength according to energy conservation ($\omega_{\text{vis}} = 2\omega_{\text{IR}}$). Here N(2N) stands for the azimuthal mode number, which is determined by momentum conservation ($m_{\text{vis}} = 2m_{\text{IR}}$) in the degenerate SPDC process. To

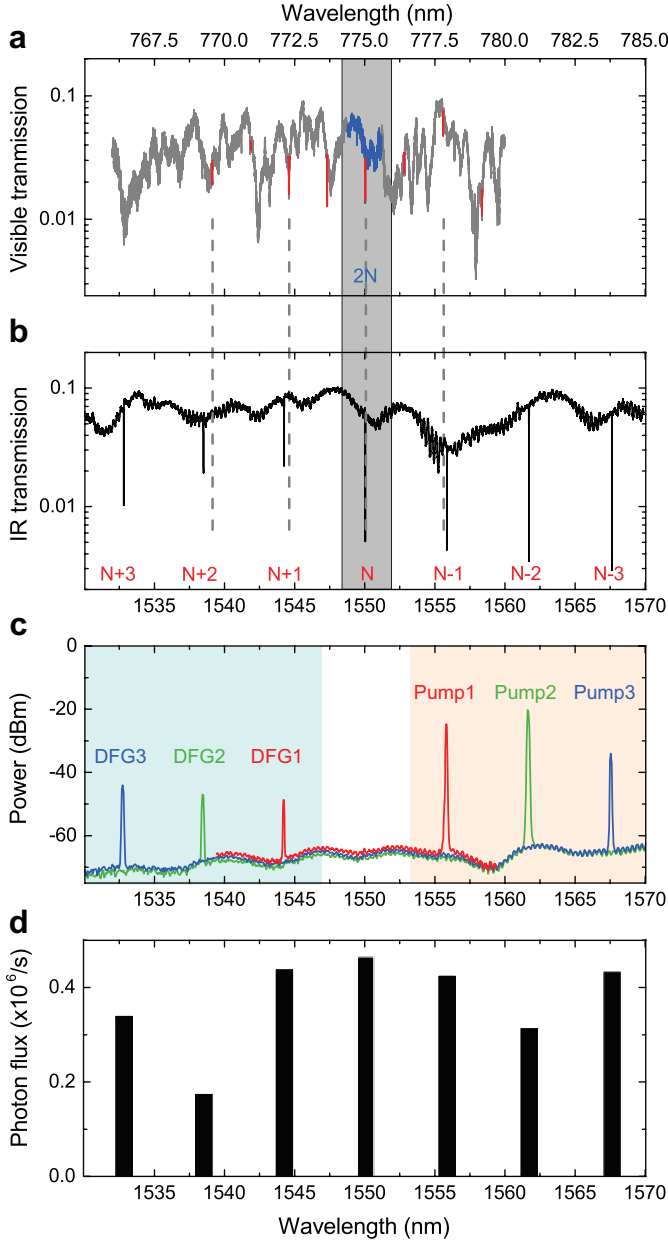


FIG. 2: Linear and nonlinear characteristics of the $\chi^{(2)}$ source. (a-b) Transmission spectra of the microring resonator. Four gray dashed lines are aligned with the visible TM_2 mode resonances. Gray region shows the phase-matched mode pair ($\text{TM}_{2,2N}$ and $\text{TM}_{0,N}$) for SHG and degenerate SPDC, whose resonances are aligned within the linewidth of IR mode resonance. (a) Visible light transmission spectrum, with TM_2 mode resonances emphasized by red lines. (b) IR light transmission spectrum, with TM_0 modes identified by the azimuthal mode number. (c) Difference frequency generation (DFG) measured by optical spectrum analyzer. Peaks due to input IR pump lasers are shown in the light orange region and generated DFG signals are shown in the light green region. Visible pump laser with 1.9 mW power on-chip is fixed on resonance with $\text{TM}_{2,2N}$ mode. (d) Single photon flux arriving at the detector chip from the degenerate and nearest three groups of non-degenerate down conversion. The counts are calibrated by the wavelength dependent detection efficiency (Supplementary Section II).

perfectly fulfill the energy conservation ($\omega_{vis} = 2\omega_{IR}$), we vary the global temperature of the chip and determine the optimized working temperature using second harmonic generation (SHG) [37, 38] as a figure of merit, which is directly related to SPDC efficiency (see theoretical derivation in supplementary section III). By pumping at $\text{TM}_{0,N}$ mode and monitoring the output SHG from $\text{TM}_{2,2N}$ mode, we observe a maximum SHG efficiency of $\eta_{SHG} = P_{SHG}/P_p^2 = 1.16 \text{ W}^{-1}$, where P_{SHG} (P_p) is the optical power of the generated second harmonic light (pump laser). Due to the group velocity mismatch between visible and IR modes, energy conservation cannot be satisfied for SHG in other modes, as can be seen in Figs. 3a and b, where no pairs of IR and visible light modes are aligned except for the $\text{TM}_{2,2N}$ and $\text{TM}_{0,N}$ modes. However, the group velocity dispersion (GVD) is relatively small in the IR region, and energy conservation can be fulfilled for IR modes over a wide wavelength range for difference/sum frequency generation (DFG/SFG) and conversely for non-degenerate SPDC. We verify this by fixing the visible wavelength pump laser at the resonance of the $\text{TM}_{2,2N}$ mode and sweep the IR probe laser over a wavelength range covering the neighboring resonances (e.g. $\text{TM}_{0,N-1}/\text{TM}_{0,N-2}/\text{TM}_{0,N-3}$ modes). We observe DFG of various modes, as shown in Fig. 2c. The fact that both SHG and various DFG-configurations can be observed indicates the possibility of generating both degenerate and non-degenerate photon-pairs in wavelength bands spaced similar to a frequency-comb.

We use SSPDs to characterize the statistical properties of photons generated by the SPDC source. In Fig. 2d the photon flux for different ring resonances is shown for fixed power and wavelength of the visible light pump laser. The variation in the detected photon rates for different resonance wavelengths can be explained by the difference in the quality factors of the IR resonator modes because the photon-pair generation rate is linearly dependent on the quality factor. As discussed in the supplementary information, the bandwidth for non-degenerate SPDC can be as large as 40 nm.

Correlated photon-pair generation

The statistical properties of the generated photon-pairs can be analyzed in terms of the second order correlation function ($g^{(2)}$), which we measure using two detectors at the outputs of a beam splitter and normalize to photon flux [43]

$$g^{(2)}(\tau) = \frac{R_{cc}(\tau)}{R_1 R_2 \tau_b} \quad (1)$$

where R_{cc} is the coincidence count rate, R_1 (R_2) is the count rate of detector 1(2), and τ_b is the coincidence time window. Here the coincidence rate R_{cc} is a function of photon-photon arrival time delay τ , while R_1 , R_2 and τ_b are constant, which combine to the accidental coincidence rate $R_{ac} = R_1 R_2 \tau_b$. We note that the $g^{(2)}(\tau)$ function is a rescale of coincidence rate $R_{cc}(\tau)$ by accidental coincidence rate R_{ac} . While the value of $R_{cc}(\tau)$ and R_{ac} are

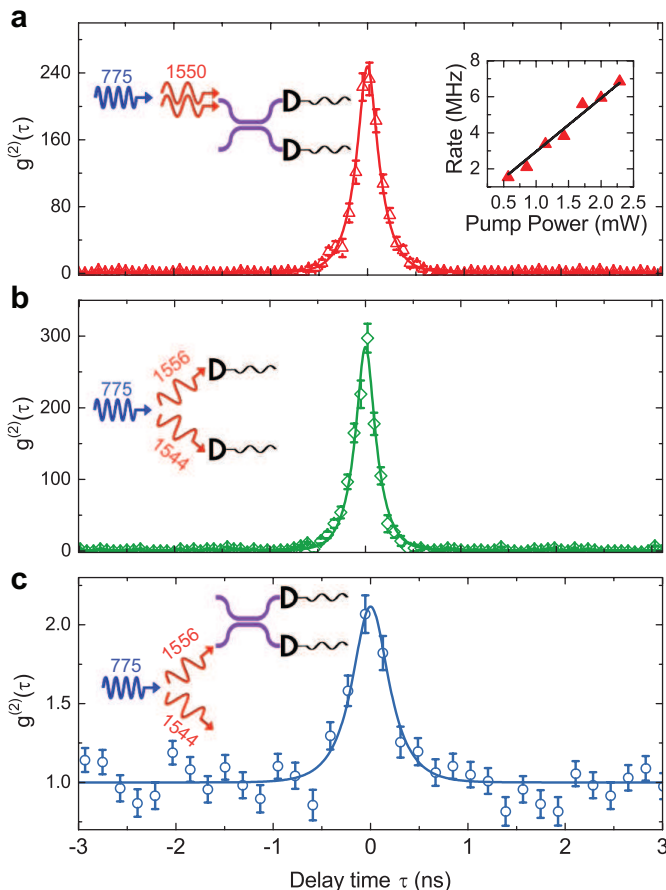


FIG. 3: Second order correlation function ($g^{(2)}(\tau)$) of down converted photons. **(a)** Self-correlation measurement of degenerate down conversion photon pairs. Right inset: Power dependence of degenerate photon pair generation rate. Normalized Generation rate of 3.0 MHz/mW has been fitted. **(b)** Cross-correlation measurement of the nearest non-degenerate down conversion photon pairs. **(c)** Self-correlation measurement of the idler in the nearest non-degenerate down conversion. The left insets in **(a-c)** show the schematics of each measurement. The solid lines are fittings with the convolution function between a double exponential decay and a Gaussian distribution function related to the chosen bin-width and detector jitter.

both dependent on the losses of the measuring systems, the value of $g^{(2)}(\tau)$ is independent of system losses, allowing us to extract the pair generation rate and SPDC photon bandwidth from the measured $g^{(2)}(\tau)$ function directly.

For degenerate SPDC photon pairs we measure the self-correlation function with two waveguide coupled SSPDs integrated with a 50/50 directional coupler, as sketched in the left inset of Fig. 3a. We observe a clear coincidence peak centered at zero delay time, which indicates strong temporal correlations between the photons emitted from the SPDC source. The second order self-correlation function for degenerate SPDC photon-pairs is

given by [44–46]

$$g_{self}^{(2)}(\tau) = 1 + \frac{1}{4R\tau_c} e^{-|\tau|/\tau_c}, \quad (2)$$

where τ is the delay time between two photons, τ_c is the coherence time of the SPDC photons, and R is the photon-pair generation rate. Here, random fluctuations in the photons arrival time ($\delta\tau$) have to be taken into account because the detector jitter (τ_j , see supplementary section V) and the coincidence time window (τ_b) are not negligible compared with the photons' coherence time (τ_c). Assuming the arrival time fluctuations $\delta\tau$ follow a normal distribution $\frac{1}{\sqrt{2\pi}\tau_w} e^{-\delta\tau^2/2\tau_w^2}$, with standard deviation $\tau_w = \sqrt{2\tau_j^2 + (\frac{\tau_b}{2})^2}$, the correlation function can be expressed as (see supplementary section V)

$$g_{self}^{(2)}(\tau) = 1 + \frac{1}{8R\tau_c} e^{\tau_w^2/2\tau_c^2} [f_+(\tau) + f_-(\tau)], \quad (3)$$

where $f_{\pm}(\tau) = \left[1 \mp \text{erf}\left(\frac{\tau \pm \tau_w^2/\tau_c}{\sqrt{2}\tau_w}\right)\right] \cdot e^{\pm\tau/\tau_c}$ and $\text{erf}(x)$ is the error function. From a fit to the data in Fig. 3a, we obtain the degenerate photon pair generation rate $R = 5.9$ MHz for 1.9 mW pump power on-chip. The bandwidth of the photons extracted from the fit to the data is $\Delta\nu = \frac{1}{2\pi\tau_c} = 1.1$ GHz, which agrees with the measured linewidth of the IR resonator mode. The photon-pair generation rate as a function of pump power is shown in the right inset of Fig. 3a. We obtain a generation rate of 3.0 MHz/mW for degenerate SPDC.

For non-degenerate SPDC photon pairs, the photons of a pair may have different wavelengths. If we discard all the signal photons and only measure the emission of idler photons, a thermal state statistics is expected [47]. We measure the self-correlation function for the nearest idler (TM_{0,N-1}) photons, as shown in the inset of Fig. 3c. We obtain $g^2(0) = 2.07 \pm 0.12$ from a fit to the data in Fig. 3c, which is in agreement with the expected value of $g^2(0) = 2$ for single mode thermal state [43, 48].

We then separate signal and idler photons by a DWDM and use two independent waveguide coupled SSPDs to measure the second order cross-correlation function between signal and idler, as shown in the inset of Fig. 3b. For non-degenerate photon pairs, the cross-correlation function is given as:

$$g_{cross}^{(2)}(\tau) = 1 + \frac{1}{4R\tau_c} e^{\tau_w^2/2\tau_c^2} [f_+(\tau) + f_-(\tau)]. \quad (4)$$

From a fit to the data in Fig. 3b we extract the photon pair generation rate of $R = 11.0$ MHz for 1.9 mW pump power (5.8 MHz/mW) and the bandwidth $\Delta\nu = \frac{1}{2\pi\tau_c} = 1.1$ GHz, which is similar to the degenerate SPDC case. We conclude that non-degenerate SPDC is around two times more efficient than degenerate SPDC, which matches well with our theoretical calculation and originates from different coefficients of interaction Hamiltonian for degenerate and non-degenerate SPDC processes

(supplementary section III). Additional cross-correlation measurements for photon pairs emitted into other microring resonance modes are shown in the supplementary information. The total (including degenerate and different groups of non-degenerate) photon pair generation rate for this AlN microring source is more than 20 MHz/mW, which is comparable or even higher than the state-of-the-art SPDC photon pair source using bulk or waveguide-based $\chi^{(2)}$ crystals [24]. In terms of the spectral brightness, AlN microring source is much brighter due to microring's narrow linewidth.

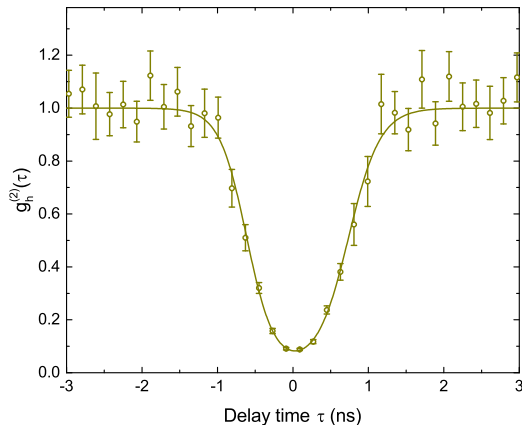


FIG. 4: Heralded signal-signal correlation function ($g_h^{(2)}(\tau)$) of down converted photons. On-chip pump power of 1.9 mW is used to get enough counting rate. Here the heralded anti-bunching dip of $g_h^{(2)}(0) = 0.088 \pm 0.004$ indicates that the photon pair source is operating in the single photon regime.

Source of heralded single photons

With 1.9 mW pump power on-chip, the photon pair generation rate for the nearest non-degenerate modes ($\text{TM}_{0,N+1}$ and $\text{TM}_{0,N-1}$) is 11.0 MHz. To further verify that our photon pair source can be used as a heralded single photon source, we measure the normalized signal-signal self-correlation function conditioned on the detection of an idler photon [44, 49]

$$g_h^{(2)}(t_{s1}, t_{s2}|t_i) = \frac{P_{ssi}(t_{s1}, t_{s2}, t_i)}{r(0)^3 g_{si}^{(2)}(t_{s1} - t_i) \cdot g_{si}^{(2)}(t_{s2} - t_i)}, \quad (5)$$

where P_{ssi} is the coincidence rate of detecting one idler and two signal photons, $g_{si}^{(2)}$ is the second order cross correlation function and $r(\tau)$ is first order correlation function [49]. Here we are interested in the special case of $g_h^{(2)}(\tau) \equiv g_h^{(2)}(0, \tau|0)$. For an ideal photon pair source, we expect to detect at most one signal photon upon detection of one (heralding) idler photon. Thus an anti-bunching dip around zero delay time ($\tau = 0$) is expected. In our experiment, we split up the nearest non-degenerate photon pairs deterministically using a DWDM. We then

use the idler photon as a herald for the detection of its partner photon and measure the autocorrelation function for the latter. Shown in Fig. 4 is the measurement result with no background noises or dark counts subtracted. We extract $g_h^{(2)}(0) = 0.088 \pm 0.004 \ll 0.5$ from the data, which confirms that our SPDC source indeed yields single photons with nonclassical correlations.

Device losses and measuring efficiencies

The raw data of the coincidence measurements is shown in the supplementary information. The measured coincidence rate is around 80 Hz. For a pump power of 1.9 mW on-chip we infer an emission rate of photon pairs in the nearest non-degenerate modes of 11.0 MHz from a fit to the coincidence data in Fig. 3b. The difference between these rates arises from losses at the various device interfaces, i.e. microring-to-waveguide (3 dB), fiber-to-chip interface (3.5 dB), silicon filter (3 dB), DWDM (6 dB) and non-ideal detector efficiency (10 dB). Without subtracting any background noise or dark counts we find a coincidence-to-accidental ratio (CAR) of 560 for a minimum pump power of 0.6 mW, at which the on-chip generation rate amounts to 3.5 MHz.

On-chip wavelength division multiplexer

The large difference in pump and signal / idler wavelengths in the SPDC process allows for a variety of design choices to separate pump light from the generated photons. One could choose to exploit wavelength selective material absorption, e.g. silicon will strongly absorb visible light but transmit IR light. Another approach is to design WDM waveguide circuits. In this work we choose to realize the latter one because a WDM structure has the additional benefit of simplifying the fiber-to-chip coupling interface: 1) When characterizing the IR and visible performances of the microring, only one optical fiber at each side of the photonic chip is needed. 2) When characterizing the down-conversion photon pairs, a single optical fiber is simultaneously used to send the pump light into and collect generated photon pairs from the chip (as shown in Fig. 1a). The designed WDM structure employs tapered waveguide couplers, as shown in Figs. 5a and b. In dielectric waveguides the optical mode confinement decreases towards longer wavelengths, such that IR light will have a longer-range evanescent field outside the waveguides as compared to visible light. For two waveguides in close proximity the resulting coupling is hence stronger for IR than for visible wavelength light. We hence adjust the coupling length such that IR light is efficiently transferred from one waveguide to another (Fig. 5a) while visible light remains unaffected and is transmitted through the coupling region without coupling to the neighboring waveguide (Fig. 5b).

Here the adiabatic taper WDM design is realized with large fabrication tolerances and broadband working wavelength. The relationship between coupling efficiency and coupling length is shown in Fig. 5c for $\lambda = 1550$ nm and $\lambda = 775$ nm. The design shown in Figs. 5a and b

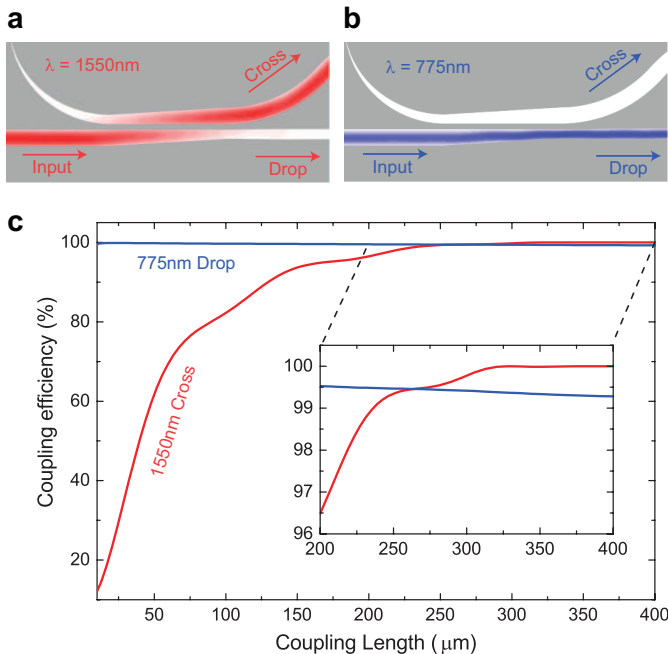


FIG. 5: On-chip wavelength division multiplexer (WDM). (a-b) Simulated electric field profiles of the designed on-chip WDM device for IR ($\lambda = 1550$ nm) and visible ($\lambda = 775$ nm) light. (c) Coupling efficiency of IR light to cross port and visible light to drop port. Inset, Zoom in of coupling efficiency for coupling length ranging from $200 \mu\text{m}$ to $400 \mu\text{m}$.

corresponds to a coupling length of $350 \mu\text{m}$ and a gap of $0.4 \mu\text{m}$. With increasing coupling length, the cross port coupling for IR light increases monotonically and saturates at 100%, while the visible light transmission into the drop port decreases linearly with coupling length but remains above 99% over the entire range. The inset of Fig. 5c shows that more than 99% coupling efficiency into the cross and drop ports are achieved simultaneously for IR and visible light, respectively, for coupling lengths ranging from $250 \mu\text{m}$ to $400 \mu\text{m}$. This performance corresponds to 20 dB suppression of visible pump light with less than 0.044 dB insertion loss for IR light for each of the on-chip WDM structures. In future implementations, a cascade of such WDMs could be used for realizing sufficient suppression of guided pump light. Note that in the current experimental configuration, a portion of the pump light is directly reflected back into the optical fiber from the fiber-to-chip interface and is thus guided towards the detectors. To suppress these residual pump photons we use an additional fiber-coupled silicon filter, i.e. off-chip.

Discussion

The high-visibility antibunching of heralded single photons shown in Fig. 4 confirms the nonclassical character of our SPDC source. However, for quantum information processing it is furthermore desirable to generate photons in a pure state [50]. We use the Schmidt number,

K , to describe any remaining entanglement between optical modes of a SPDC pair. Schmidt number K , heralded single photon state purity P and the second order self-correlations are related via $g^{(2)}(0) = 1 + 1/K = 1 + P$ [48, 50]. Ideal heralded purity ($P = 1$) is obtained if all measured photons are found in the same optical mode ($K = 1$). Conversely, if photons are found in multiple output modes ($K \gg 1$), the correlation function $g^{(2)}(0)$ approaches 1 and the heralded purity approaches 0. In our experimental configuration, down-converted photons will only be emitted into TM_0 modes because other spatial modes do not fulfill the phase matching condition. These TM_0 modes are spectrally separated by at least one free spectral range (FSR), as shown in Fig. 2d. Selecting one of these modes with a bandpass filter thus yields single mode emission. The measured $g^2(0) = 2.07 \pm 0.12$ ($P = 1.07 \pm 0.12$) in Fig. 3c confirms that single mode emission and nearly ideal (unit) heralded purity are indeed achieved by our SPDC source.

In addition to the purity of generated photons, sufficient on-chip pump rejection is a key requirement for achieving source-detector integration on the same chip. Here we discuss the prospects of realizing sufficient on-chip filtering. 1) Suppressing guided pump light in photonic waveguide circuits: The filtering of pump photons propagating inside a waveguide could for example be achieved by depositing a thin layer of silicon on top of the waveguide interfacing source (circuit) and detector. Silicon has an absorption coefficient of 1740 dB/cm for the pump wavelength (775 nm) at cryogenic temperatures, while being transparent for down-converted photons (around 1550 nm). The hybrid AlN-silicon waveguide hence results in great selective absorption of pump photons. Alternatively, five cascaded on-chip WDMs (as described above) could also provide efficient pump light rejection. 2) Suppressing unguided pump photons propagating in free-space, substrate and cladding materials: Photons incident from free space can efficiently be absorbed in a metal layer covering the area where detectors are located [51]. Pump photons scattered into a transparent substrate on the other hand pose a significant challenge in SFWM experiments, where the pump light in telecom band near 1550 nm can propagate losslessly in the cladding (usually SiO_2) and substrate (usually silicon) materials and finally couple to the detection region, limiting the on-chip filter's performance [32]. In our case, however, the visible pump photons scattered into the silicon substrate layer are efficiently absorbed due to large material absorption. Pump photons coupled directly from the input fiber into SiO_2 slab modes may propagate for somewhat longer distances before leaking into the underlying silicon substrate of higher refractive index. Numerical simulations show that the attenuation of slab modes is $\geq 90(200)$ dB/cm for a $3(2) \mu\text{m}$ thick SiO_2 buffer layer. Hence, detectors can be efficiently shielded from pump photons propagating inside the cladding layer if they are separated by a centimeter from the fiber-to-chip interface.

AlN has a $\chi^{(2)}$ coefficient (4.7 pm/V) [38] which is almost ten times smaller than that of LiNbO₃ (41.7 pm/V) [52]. However, using advanced nanofabrication techniques we are able to realize microring resonators with high quality factors, which results in a resonant pump power enhancement that compensates for the weaker nonlinear coefficient. This is confirmed by comparing the SHG efficiency achieved in our AlN-device (1.16 W^{-1}) to recently reported SHG efficiencies in LiNbO₃ micro disks (0.109 W^{-1}) [52, 53]. We see potential for further enhancing the nonlinear conversion efficiency for AlN microring resonators by decreasing the ring radius and improving the quality factor of the microring resonator. We believe that five times higher quality factors and a three-fold decrease in radius are achievable in future AlN devices, which brings SHG efficiencies of 400 W^{-1} within reach.

CONCLUSIONS

In conclusion, the demonstrated photon pair source based on the $\chi^{(2)}$ nonlinearity of AlN microring resonators and the quantum correlation measurement with waveguide-integrated single-photon detectors constitute an exciting step towards fully integrated quantum photonic circuits. Compared to photonic circuits fabricated from

more traditional semiconductor materials, e.g. silicon-on-insulator, AlN permits high quality (high brightness, high purity, low noise) correlated photon pair emission spectrally far separated from the pump light. AlN-on-insulator therefore holds great potential for realizing efficient pump suppression and monolithic integration of non-classical light sources with single photon detectors on the same chip. Additionally, high-speed phase modulation via the electro-optic effect will enable real-time circuit reconfiguration. In combination with high-efficiency single-photon detectors it will thus be possible to generate non-classical photonic states and implement feed-forward schemes as well as quantum logic operations in a scalable manner.

Acknowledgments

H.X.T. acknowledges support from a Packard Fellowship in Science and Engineering. C.S. acknowledges financial support from the Deutsche Forschungsgemeinschaft (SCHU 2871/2-1). Facilities used for fabrication were supported by Yale SEAS cleanroom and Yale Institute for Nanoscience and Quantum Engineering. The authors thank Michael Power and Dr. Michael Rooks for assistance in device fabrication.

-
- [1] Kok, P. et al. Linear optical quantum computing with photonic qubits. *Rev. Mod. Phys.* 79, 135–174 (2007).
 - [2] O’Brien, J. L., Furusawa, A. & Vuckovic, J. Photonic quantum technologies. *Nature Photon.* 3, 687–695 (2009).
 - [3] Burnham, D. C. & Weinberg, D. L. Observation of Simultaneity in Parametric Production of Optical Photon Pairs. *Phys. Rev. Lett.* 25, 84–87 (1970).
 - [4] Kwiat, P. G. et al. New High-Intensity Source of Polarization-Entangled Photon Pairs. *Phys. Rev. Lett.* 75, 4337–4341 (1995).
 - [5] Bouwmeester, D., Pan, J.-W., Mattle, K., Eibl, M., Weinfurter, H., Zeilinger, A. Experimental quantum teleportation. *Nature* 390, 575–579 (1997).
 - [6] Ma, X.-S. et al. Quantum teleportation between the Canary Islands La Palma and Tenerife over both quantum and classical 143-km free-space channels. *Nature* 489, 269–273 (2012).
 - [7] Bussi eres, F. et al. Quantum teleportation from a telecom-wavelength photon to a solid-state quantum memory. *Nature Photon.* 8, 775–778 (2014).
 - [8] Peruzzo, A. et al. Quantum Walks of Correlated Photons. *Science* 329, 1500–1503 (2010).
 - [9] Matthews, J. C. F., Politi, A., Stefanov, A. & O’Brien, J. L. Manipulation of multiphoton entanglement in waveguide quantum circuits. *Nature Photon.* 3, 346–350 (2009).
 - [10] Shadbolt, J. et al. Generating, manipulating and measuring entanglement and mixture with a reconfigurable photonic circuit. *Nature Photon.* 6, 45–49 (2012).
 - [11] Huang, Y.-F. et al. Experimental generation of an eight-photon Greenberger–Horne–Zeilinger state. *Nature Commun.* 2, 546 (2011).
 - [12] Pan, J.-W. et al. Multiphoton entanglement and interferometry. *Rev. Mod. Phys.* 84, 777–838 (2012).
 - [13] Spring, J. B. et al. Boson Sampling on a Photonic Chip. *Science* 339, 798–801 (2013).
 - [14] Broome, M. A. et al. Photonic Boson Sampling in a Tunable Circuit. *Science* 339, 794–798 (2013).
 - [15] Lu, C.-Y., Browne, D. E., Yang, T. & Pan, J.-W. Demonstration of a Compiled Version of Shor’s Quantum Factoring Algorithm Using Photonic Qubits. *Phys. Rev. Lett.* 99, 250504 (2007).
 - [16] Lanyon, B. P. et al. Experimental Demonstration of a Compiled Version of Shor’s Algorithm with Quantum Entanglement. *Phys. Rev. Lett.* 99, 250505 (2007).
 - [17] Politi, A., Matthews, J. C. F. & O’Brien, J. L. Shor’s Quantum Factoring Algorithm on a Photonic Chip. *Science* 325, 1221 (2009).
 - [18] Martin-Lopez, E. et al. Experimental realization of Shor’s quantum factoring algorithm using qubit recycling. *Nature Photon.* 6, 773–776 (2012).
 - [19] Zhou, X., Kalasuwan, P., Ralph, T. & O’Brien, J. Calculating unknown eigenvalues with a quantum algorithm. *Nature Photon.* 7, 223–228 (2013).
 - [20] Giustina, M., et al. Significant-Loophole-Free Test of Bell’s Theorem with Entangled Photons. *Phys. Rev. Lett.* 115, 250401 (2015).
 - [21] Shalm, L. K., et al. Strong Loophole-Free Test of Local Realism. *Phys. Rev. Lett.* 115, 250402 (2015).
 - [22] Kruse, R. et al. Spatio-spectral characteristics of parametric down-conversion in waveguide arrays. *New J. Phys.* 15, 083046 (2013).
 - [23] Solntsev, A. S. et al. Generation of Nonclassical Biphoton States through Cascaded Quantum Walks on a Nonlinear Chip. *Phys. Rev. X* 4, 31007 (2014).
 - [24] Jin, H. et al. On-Chip Generation and Manipulation of Entangled Photons Based on Reconfigurable Lithium-

- Niobate Waveguide Circuits. *Phys. Rev. Lett.* 113, 103601 (2014).
- [25] Tanzilli, S. et al. On the genesis and evolution of Integrated Quantum Optics. *Laser Photon. Rev.* 6, 115–143 (2012).
- [26] Politi, A., Cryan, M. J., Rarity, J. G., Yu, S. & O’Brien, J. L. Silica-on-Silicon Waveguide Quantum Circuits. *Science* 320, 646–649 (2008).
- [27] Pernice, W. H. P. et al. High-speed and high-efficiency travelling wave single-photon detectors embedded in nanophotonic circuits. *Nature Commun.* 3, 1325 (2012).
- [28] Schuck, C., Guo, X., Fan, L., Ma, X., Poot, M., Tang, H. X., Quantum interference in heterogeneous superconducting-photonic circuits on a silicon chip. *Nature Comm.* 7, 10352 (2016).
- [29] Sharping, J. E. et al. Generation of correlated photons in nanoscale silicon waveguides. *Opt. Express* 14, 12388 (2006).
- [30] Clemmen, S. et al. Continuous wave photon pair generation in silicon-on-insulator waveguides and ring resonators. *Opt. Express* 17, 16558–70 (2009).
- [31] Silverstone, J. W. et al. On-chip quantum interference between silicon photon-pair sources. *Nature Photon.* 8, 104–108 (2014).
- [32] Harris, N. C. et al. Integrated Source of Spectrally Filtered Correlated Photons for Large-Scale Quantum Photonic Systems. *Phys. Rev. X* 4, 041047 (2014).
- [33] Collins, M. J. et al. Integrated spatial multiplexing of heralded single-photon sources. *Nature Commun.* 4, 2582 (2013).
- [34] Matsuda, N. et al. A monolithically integrated polarization entangled photon pair source on a silicon chip. *Sci. Rep.* 2, 817 (2012).
- [35] Rassani, D. A. G. et al. Micrometer-scale integrated silicon source of time-energy entangled photons. 2, 88–94 (2015).
- [36] Silverstone, J. W. et al. Qubit entanglement between ring-resonator photon-pair sources on a silicon chip. *Nature Commun.* 6, 7948 (2015).
- [37] Xiong, C. et al. Aluminum nitride as a new material for chip-scale optomechanics and nonlinear optics. *New J. Phys.* 14, 95014 (2012).
- [38] Pernice, W. H. P., Xiong, C., Schuck, C. & Tang, H. X. Second harmonic generation in phase matched aluminum nitride waveguides and micro-ring resonators. *Appl. Phys. Lett.* 100, 223501 (2012).
- [39] Yang, Z. & Sipe, J. E. Generating entangled photons via enhanced spontaneous parametric downconversion in AlGaAs microring resonators. *Opt. Lett.* 32, 3296–3298 (2007).
- [40] Schuck, C., Pernice, W. H. P. & Tang, H. X. Waveguide integrated low noise NbTiN nanowire single-photon detectors with milli-Hz dark count rate. *Sci. Rep.* 3, 1893 (2013).
- [41] Levy, J. S., Foster, M. A., Gaeta, A. L. & Lipson, M. Harmonic generation in silicon nitride ring resonators. *Opt. Express* 19, 11415–21 (2011).
- [42] Schuck, C., Pernice, W. H. P., Ma, X. & Tang, H. X. Optical time domain reflectometry with low noise waveguide-coupled superconducting nanowire single-photon detectors. *Appl. Phys. Lett.* 102, 191104 (2013).
- [43] Förtsch, M. et al. Highly efficient generation of single-mode photon pairs from a crystalline whispering-gallery-mode resonator source. *Phys. Rev. A* 91, 23812 (2015).
- [44] Förtsch, M. et al. A versatile source of single photons for quantum information processing. *Nature Commun.* 4, 1818 (2013).
- [45] Reimer, C. et al. Integrated frequency comb source of heralded single photons. *Opt. Express* 22, 6535–46 (2014).
- [46] Clausen, C. et al. A source of polarization-entangled photon pairs interfacing quantum memories with telecom photons. *New J. Phys.* 16, 93058 (2014).
- [47] Blauensteiner, B., Herbauts, I., Bettelli, S., Poppe, A. & Hübner, H. Photon bunching in parametric downconversion with continuous-wave excitation. *Phys. Rev. A* 79, 063846 (2009).
- [48] Christ, A., Laiho, K., Eckstein, A., Cassemiro, K. N. & Silberhorn, C. Probing multimode squeezing with correlation functions. *New J. Phys.* 13, 33027 (2011).
- [49] Bettelli, S. Comment on "Coherence measures for heralded single-photon sources". *Phys. Rev. A* 81, 37801 (2010).
- [50] Spring, J. B. et al. On-chip low loss heralded source of pure single photons. *Opt. Express* 21, 13522–13532 (2013).
- [51] Reithmaier, G. et al. On-Chip Generation, Routing, and Detection of Resonance Fluorescence. *Nano Lett.* 15, 5208–5213 (2015).
- [52] Wang, C. et al. Integrated high quality factor lithium niobate microdisk resonators. *Opt. Express* 22, 30924–30933 (2014).
- [53] Lin, J. et al. Fabrication of high-Q lithium niobate microresonators using femtosecond laser micromachining. *Sci. Rep.* 5, 8072 (2015).